


Spontaneous spin splitting in electric potential difference antiferromagnetism

San-Dong Guo^{1,*} and Yee Sin Ang²

¹*School of Electronic Engineering, Xi'an University of Posts and Telecommunications, Xi'an 710121, China*

²*Science, Mathematics and Technology (SMT), Singapore University of Technology and Design, 487372 Singapore*

 (Received 12 July 2023; revised 29 September 2023; accepted 21 October 2023; published 6 November 2023)

Antiferromagnetic (AFM) materials are robust to external magnetic perturbation due to the absence of net magnetic moment, which also eliminates spin splitting in the band structures. Altermagnetism provides a route to resurrect the spin-split bands in a collinear symmetry-compensated antiferromagnet with special magnetic space group. Here we propose an alternative mechanism to achieve spin splitting in a two-dimensional (2D) Janus A-type AFM material. Since the built-in electric field intrinsic to the Janus structure creates a layer-dependent electrostatic potential, the electronic bands in different layers stagger to produce the spin-splitting effect, resulting in the electric potential difference antiferromagnetism (EPD-AFM). We demonstrate that Janus monolayer Mn₂CIF is a candidate material for achieving EPD-AFM by first-principles calculations. We further show that the spin splitting in EPD-AFM can be tuned by the piezoelectric effect. This work reveals a different class of 2D AFM materials with spin polarization.

DOI: [10.1103/PhysRevB.108.L180403](https://doi.org/10.1103/PhysRevB.108.L180403)

Introduction. Spin splitting in a band structure can be produced via spin-orbit coupling (SOC) [1]. The SOC Hamiltonian H_{SOC} in a solid-state material with a lack of inversion symmetry and can be generally expressed as [2,3]

$$H_{\text{SOC}} = \vec{\Omega}(\vec{k}) \cdot \vec{\sigma} = \alpha(\vec{E} \times \vec{k}) \cdot \vec{\sigma}, \quad (1)$$

where $\vec{\Omega}(\vec{k})$ is the spin-orbit field (SOF) which acts as an effective magnetic field, α is the strength of the SOC, \vec{E} is the local electric field induced by the crystal inversion asymmetry, \vec{k} is the wave vector, and $\vec{\sigma} = (\sigma_x, \sigma_y, \sigma_z)$ are the Pauli matrices.

If a two-dimensional (2D) material possesses an out-of-plane built-in electric field, Eq. (1) leads to the Rashba SOC Hamiltonian [4],

$$H_{\text{SOC}}^{E_z} = \alpha_R(k_x\sigma_y - k_y\sigma_x), \quad (2)$$

where α_R is the so-called Rashba parameter. Here, the spin S only has the in-plane components, S_x and S_y , which depend on the momentum of the electrons. Scattering by impurities and defects can change the momentum of electrons, which randomizes the spin due to the k -dependent SOF and leads to spin decoherence through the Dyakonov-Perel (DP) mechanism [5]. In contrast, if a 2D material possesses an in-plane built-in electric field, for example along the x direction, Eq. (1) is reduced to

$$H_{\text{SOC}}^{E_x} = \alpha_D k_y \sigma_z. \quad (3)$$

Here, the spin S only has the out-of-plane component S_z . The SOF orientation of Eq. (3) is unidirectional, which leads to a spatially periodic mode of spin polarization, known as the persistent spin helix (PSH) [6,7]. The PSH can suppress

spin dephasing due to the SU(2) spin rotation symmetry, thus producing an extremely long spin lifetime [6,8].

Beyond SOC, spin splitting can also be realized *spontaneously* in ferromagnetic (FM) materials. FM materials are, however, subject to external magnetic perturbation. In contrast, antiferromagnetic (AFM) materials are inherently robust to external magnetic perturbation due to the absence of magnetic moment, and represent a key to high-speed and high-density device applications [9,10]. However, the lack of spin splitting in AFM materials severely limits their potential in spintronics applications. Spin splitting can be resurrected in a collinear symmetry-compensated AFM system, known as the altermagnetism [11–13], which has been predicted in several 2D materials, such as Cr₂O₂ [14,15], Cr₂SO [16], and V₂Se₂O [17]. Spontaneous antisymmetric spin splitting in noncollinear antiferromagnets without SOC has also been reported [18]. Ba₃MnNb₂O₉ exhibits the 120°-AFM structure with out-of-plane cantings on the triangular lattice at low temperatures [19], and the first-principles calculations show the spin splitting in the band structures without including SOC [18].

Here, we propose a different mechanism to achieve spin splitting in AFM materials. In a typical 2D material with out-of-plane inversion symmetry, the magnetic atoms have opposite layer spin polarization, namely, A-type AFM ordering. The band structures are spin degenerate [Figs. 1(a) and 1(b)]. In a 2D Janus material with A-type AFM ordering, the built-in out-of-plane electric field E_b arising from the broken out-of-plane inversion symmetry destroys the spin degeneracy in the band structures [Figs. 1(c) and 1(d)]. Such spin-degeneracy breaking arises from the layer-dependent electrostatic potential created by the built-in electric field, which causes the electronic bands in different layers to stagger and gives rise to the spin-splitting effect. We denote such system as the *electric potential difference antiferromagnetism* (EPD-AFM), which

*sandongyuwang@163.com

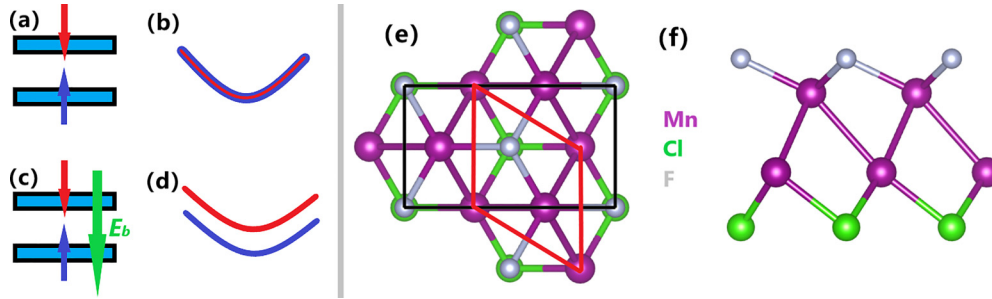


FIG. 1. (a) In a 2D material without inversion symmetry breaking, the magnetic atoms have opposite layer spin polarization (A-type antiferromagnetic ordering) which leads to (b) spin-degenerate bands. (c) In a 2D Janus material with A-type AFM ordering, the out-of-plane built-in electric field E_b destroys the spin degeneracy of the bands (d). (e), (f) The top and side views of Janus monolayer Mn_2ClF . In (e), the rhombus primitive cell (rectangle supercell) is marked by the red (black) frame.

provides an alternative route to simultaneously achieve both spontaneous spin splitting and AFM ordering.

Motivated by the recent demonstration of electric field control of spin polarization in a 2D A-type AFM Mn_2Cl_2 and the achievement of 100% spin polarization via an electric field [20], we show that the Janus counterpart, i.e., Mn_2ClF , constructed by replacing one of the two Cl layers with F atoms, is a candidate material to achieve EPD-AFM by first-principles calculations. We show that EPD-AFM in Mn_2ClF is robust against the electronic correlation. The piezoelectric properties of Mn_2ClF are also investigated, and the out-of-plane piezoelectric response may be used to tune the spin splitting. These findings reveal a different type of spin-splitting phenomenon via the synergy of AFM and broken inversion symmetry in 2D Janus materials, and may lead to a new family of magnetic materials for spintronic devices applications.

Computational details. Within density functional theory (DFT) [21], the spin-polarized first-principles calculations are carried out within the projector augmented-wave (PAW) method by using the standard VASP code [22–24]. We use the generalized gradient approximation of Perdew-Burke-Ernzerhof (PBE-GGA) [25] as the exchange-correlation functional. To account for the electron correlation of Mn-3d orbitals, we use a Hubbard correction, $U_{\text{eff}} = 4.00$ eV, within the rotationally invariant approach proposed by Dudarev *et al.*, which has been widely used in different magnetic systems containing Mn atoms [26–29]. The kinetic energy cutoff of 500 eV, total energy convergence criterion of 10^{-8} eV, and force convergence criterion of 0.0001 eV \AA^{-1} are set to obtain the accurate results. A vacuum of more than 16 \AA is used to avoid out-of-plane interaction. The elastic stiffness tensor C_{ij} and piezoelectric stress tensor e_{ij} are calculated by using the strain-stress relationship (SSR) method and density functional perturbation theory (DFPT) method [30], respectively. The C_{ij}^{2D}/e_{ij}^{2D} has been renormalized by $C_{ij}^{2D} = L_z C_{ij}^{3D}/e_{ij}^{2D} = L_z e_{ij}^{3D}$, where the L_z is the length of unit cell along the z direction. We use a $21 \times 21 \times 1$ k -point mesh to sample the Brillouin zone (BZ) for calculating electronic structures and elastic properties, and a $10 \times 21 \times 1$ k -point mesh for piezoelectric calculations. The interatomic force constants (IFCs) are calculated by using a $5 \times 5 \times 1$ supercell within the finite displacement method, and the phonon dispersion spectrum can be calculated by the PHONOPY code [31]. The

elastic, piezoelectric, phonon, and *ab initio* molecular dynamics (AIMD) calculations are all performed with AFM1 magnetic configuration.

Crystal structure and stability. The 2D Janus materials have asymmetric facial properties with unique properties such as an out-of-plane piezoelectric polarization, the second harmonic generation response, and strong Rashba effect due to their out-of-plane asymmetry [32]. The MoS₂ as a representative 2D Janus material has been experimentally achieved [33,34].

Monolayer Mn_2ClF possesses similar crystal structures as Mn_2Cl_2 [20], i.e., the four-atomic layer sequence of Cl-Mn-Mn-F [see Figs. 1(e) and 1(f)]. An intrinsic polar electric field along the out-of-plane direction is induced by the electronegativity difference of the Cl and F elements, which provides the basis for realizing EPD-AFM. Non-Janus Mn_2Cl_2 possesses the $P\bar{3}m1$ space group (no. 164), and the space group of Mn_2ClF is reduced to $P3m1$ (no. 156) due to broken out-of-plane mirror symmetry. Such symmetry breaking also leads to in-plane and out-of-plane piezoelectricity, as shown below.

To determine the magnetic ground state of Mn_2ClF , a rectangular supercell [see Fig. 1(e)] is used to construct an FM and three AFM configurations (AFM1, AFM2, and AFM3). These magnetic configurations are shown in Fig. 2. The AFM1 is known as the A-type AFM state, which is the ground state of Mn_2ClF as its energy per unit cell is 0.43 eV, 0.32 eV, and 0.23 eV lower than those of FM, AFM2, and AFM3,

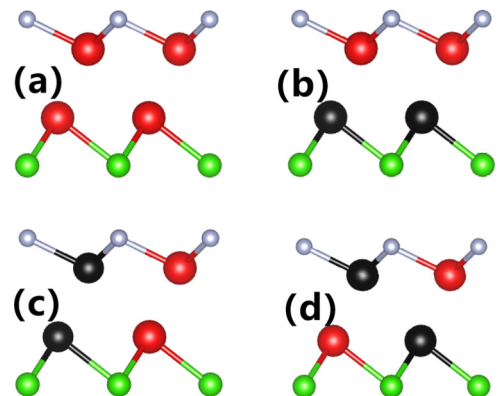


FIG. 2. For monolayer Mn_2ClF , (a) the FM, and three AFM configurations: (b) AFM1, (c) AFM2, and (d) AFM3.

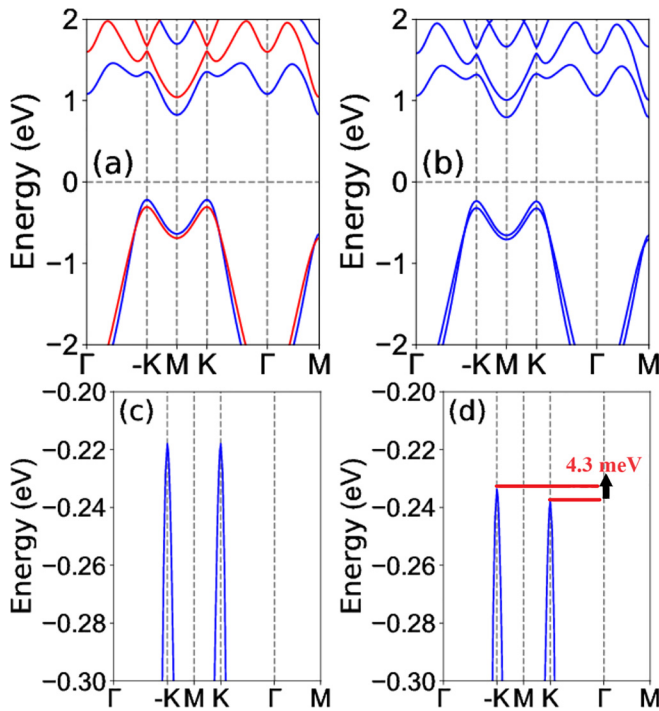


FIG. 3. Energy band structures of Mn_2ClF (a) without SOC and (b) with SOC. In (a), the spin-up and spin-down channels are depicted in blue and red, respectively. (c), (d) The partially enlarged view of (a) and (b) around the valence band edges.

respectively, based on GGA + U calculations. The optimized lattice constant is $a = b = 3.43 \text{ \AA}$ (GGA + U) for the AFM1 case. The magnetic easy axis is confirmed by the magnetic anisotropy energy (MAE), which is defined as the energy difference of the magnetization orientation along the (100) and (001) cases within SOC. The calculated MAE is only $1 \mu\text{eV}/\text{Mn}$, which indicates that the easy axis of Mn_2ClF is out of plane.

To validate the dynamic, thermal, and mechanical stabilities of Mn_2ClF , the phonon spectra, AIMD, and elastic constants are calculated, respectively (see Supplemental Material [35]). The calculated phonon spectrum of Mn_2ClF has no obvious imaginary frequencies, indicating its dynamic stability. The AIMD simulations using an NVT ensemble are performed for more than 8000 fs with a time step of 1 fs using a $4 \times 4 \times 1$ supercell at 300 K. During the simulation, the crystal structures of Mn_2ClF are retained without structural fracture and the energies are stable, thus confirming the thermal stability. Two independent elastic constants, C_{11} and C_{12} , of Mn_2ClF are 56.66 Nm^{-1} and 17.22 Nm^{-1} , which satisfy the Born criteria of mechanical stability, i.e., $C_{11} > 0$ and $C_{11} - C_{12} > 0$ [36], thus further confirming the mechanical stability.

Electronic structures. The magnetic moments of the bottom and top Mn atoms are 4.57 and $-4.52 \mu_B$, and the total magnetic moment per unit cell is strictly $0.00 \mu_B$. In general, the AFM material exhibits no spin splitting. However, our proposed Mn_2ClF shows obvious spin splitting in the band structures without SOC in Fig. 3(a). This is very different from that of the non-Janus counterpart Mn_2Cl_2 (see Supplemental

Material [35]), where no spin splitting exists. This difference arises from the out-of-plane polar electric field in Mn_2ClF due to its Janus morphology—a feature that is absent in Mn_2Cl_2 . In fact, if a 2D A-type AFM Mn_2Cl_2 without intrinsic spin splitting is grown on the substrate, the spin splitting will be produced due to the external Janus feature. However, the magnitude of spin splitting depends on the substrate and the spin splitting may be very small. Janus AFM Mn_2ClF provides an intrinsic spin splitting, which facilitates practical device applications.

The Mn_2ClF is an indirect band-gap semiconductor with a gap value of 1.043 eV . The valence band maximum (VBM) and conduction band minimum (CBM) are at the high-symmetry $K/-K$ and M points, respectively, and are dominantly composed of the spin-up subbands. When including the SOC, the band structures exhibit very small changes, with a slightly reduced indirect band-gap value of 1.028 eV [Fig. 3(b)]. Based on magnetic moments of Mn atoms, the valence state of the Mn ions should be Mn^{2+} . The $3d$ orbital states of Mn^{2+} would be nearly half filled so that they are hardly influenced by the SOC. Without considering SOC, the K and $-K$ valleys of the valence bands are exactly degenerate [Fig. 3(c)]. However, when SOC is switched on, the degeneracy between the K and $-K$ valleys is lifted due to broken space- and time-inversion symmetries, leading to an interesting phenomenon of the spontaneous valley polarization with very small valley splitting of 4.3 meV [Fig. 3(d)]. This is different from the common valley splitting in FM materials [37]. Recently, the spontaneous valley polarization has also been predicted in 2D AFM $\text{Mn}_2\text{P}_2\text{S}_3\text{Se}_3$ with a valley splitting of 16.3 meV [38]. For Mn_2ClF , the band structures projected onto Mn- d orbital states of different layers without SOC and with SOC are plotted in Fig. 4. Here, the weightages of the spin-up and spin-down subbands of both valence and conduction bands are reversed in different Mn layers [Figs. 4(a) and 4(b)], which gives rise to the obvious spin splitting. Here the two Mn layers are nonequivalent due to a layer-dependent electrostatic potential caused by the built-in electric field [Fig. 4(c)].

The electronic correlation can produce important effects on the magnetic ground state, electronic structures, and topological properties of 2D magnetic materials [39–43]. To confirm the robustness of EPD-AFM, the electronic correlation effects on Mn_2ClF are investigated using different U values. First, the lattice constants a of Mn_2ClF are optimized by GGA + U (0 – 5 eV) and then the related physical properties are recalculated. The lattice constants a (3.286 – 3.447 \AA) increase with increasing U (see Supplemental Material [35]). To achieve EPD-AFM, the AFM1 magnetic configuration as the ground state of Mn_2ClF is a crucial factor. The energy differences between FM/AFM2/AFM3 and AFM1 (per unit cell) as a function of U are plotted in Fig. 5, which demonstrates that Mn_2ClF is always in the AFM1 ground state within the considered U range. The evolution of the band structures as a function of U is plotted in Fig. 6 (see Supplemental Material for the gap value vs U [35]). Within the considered U range, Mn_2ClF is always an indirect gap semiconductor and exhibits obvious spin splitting. The VBM and CBM remain at the high-symmetry $K/-K$ and M points and are similarly dominated by the spin-up subbands. Finally, the MAE as a

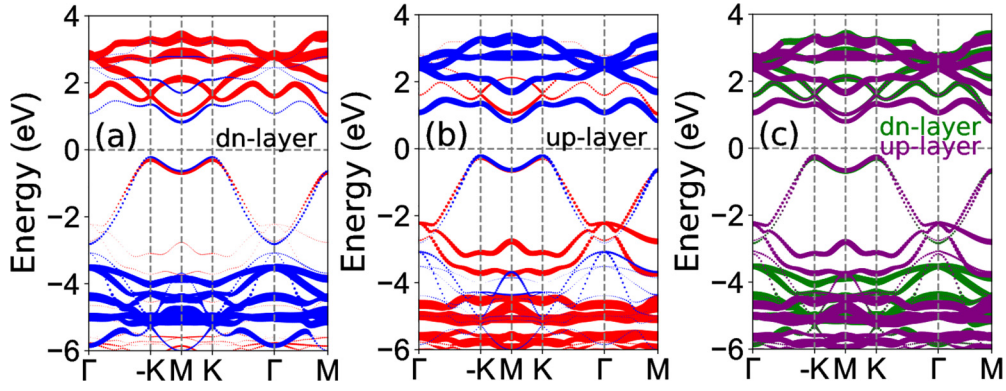


FIG. 4. Layer-characters energy band structures of Mn_2ClF without SOC (a and b) and with SOC (c). In (a) and (b), the spin-up and spin-down bands are depicted in blue and red, respectively. In (c), the spin-up and spin-down channels are not distinguished.

function of U is plotted in the Supplemental Material [35]. When $U < 4.7$ eV, the out-of-plane magnetic anisotropy is maintained. The above analysis demonstrates the robustness of EPD-AFM in Mn_2ClF .

Piezoelectric properties. The Mn_2Cl_2 monolayer possesses no piezoelectricity because of the inversion symmetry. However, due to the broken horizontal mirror symmetry, monolayer Mn_2ClF exhibits both in-plane and out-of-plane piezoelectricity. The piezoelectric response of a material can be described by the third-rank piezoelectric stress tensor e_{ijk} and strain tensor d_{ijk} , which can be expressed as the sum of the ionic and electronic contributions:

$$\begin{aligned} e_{ijk} &= \frac{\partial P_i}{\partial \varepsilon_{jk}} = e_{ijk}^{elc} + e_{ijk}^{\text{ion}}, \\ d_{ijk} &= \frac{\partial P_i}{\partial \sigma_{jk}} = d_{ijk}^{elc} + d_{ijk}^{\text{ion}}, \end{aligned} \quad (4)$$

where P_i , ε_{jk} , and σ_{jk} are the polarization vector, strain, and stress, respectively. The $i, j, k \in 1, 2, 3$, with 1, 2, and 3 corresponding to x, y , and z , respectively. The superscripts *elc/ion* denotes electronic/ionic contributions. The e_{ijk}^{elc} and d_{ijk}^{elc} are the clamped-ion piezoelectric coefficients, while the e_{ijk} and d_{ijk} are the relaxed-ion counterparts. The e_{ijk} is related to d_{ijk}

by the elastic tensor C_{mnjk} ,

$$e_{ijk} = \frac{\partial P_i}{\partial \varepsilon_{jk}} = \frac{\partial P_i}{\partial \sigma_{mn}} \frac{\partial \sigma_{mn}}{\partial \varepsilon_{jk}} = d_{imn} C_{mnjk}. \quad (5)$$

Using Voigt notation and only considering the in-plane strain and stress [44–46], Eq. (5) with $P3m1$ symmetry can be reduced to

$$\begin{pmatrix} e_{11} & -e_{11} & 0 \\ 0 & 0 & -e_{11} \\ e_{31} & e_{31} & 0 \end{pmatrix} = \begin{pmatrix} d_{11} & -d_{11} & 0 \\ 0 & 0 & -2d_{11} \\ d_{31} & d_{31} & 0 \end{pmatrix} \times \begin{pmatrix} C_{11} & C_{12} & 0 \\ C_{12} & C_{11} & 0 \\ 0 & 0 & (C_{11} - C_{12})/2 \end{pmatrix}. \quad (6)$$

With a uniaxial in-plane strain, both in-plane and out-of-plane piezoelectric polarization are produced (i.e., $e_{11}/d_{11} \neq 0$ and $e_{31}/d_{31} \neq 0$). However, when a biaxial in-plane strain is applied, the in-plane component disappears ($e_{11}/d_{11} = 0$), but the out-of-plane component may still exist ($e_{31}/d_{31} \neq 0$). By solving Eq. (6), the two independent d_{11} and d_{31} are

$$d_{11} = \frac{e_{11}}{C_{11} - C_{12}} \quad \text{and} \quad d_{31} = \frac{e_{31}}{C_{11} + C_{12}}. \quad (7)$$

The orthorhombic supercell [see Fig. 1(e)] is used to calculate the e_{11}/e_{31} of Mn_2ClF . The calculated e_{11}/e_{31} is $-0.745 \times 10^{-10} / -0.191 \times 10^{-10}$ C/m, with the ionic part $-0.647 \times 10^{-10} / 0.372 \times 10^{-10}$ C/m and the electronic part $-0.098 \times 10^{-10} / -0.563 \times 10^{-10}$ C/m. For e_{11} , the same signs can be observed for the electronic and ionic contributions. The ionic part thus plays a decisive role here. However, for e_{31} , the electronic and ionic contributions have opposite signs and the electronic part dominates the piezoelectricity. From Eq. (7), d_{11} and d_{31} of Mn_2ClF are -1.89 and -0.26 pm/V, respectively. The predicted $|d_{31}|$ is thus higher than or comparable to those of other 2D materials [44–46]. It is important to note that when a biaxial in-plane strain is imposed, only the out-of-plane d_{31} appears and an out-of-plane electric field can be induced, which can be used to tune the

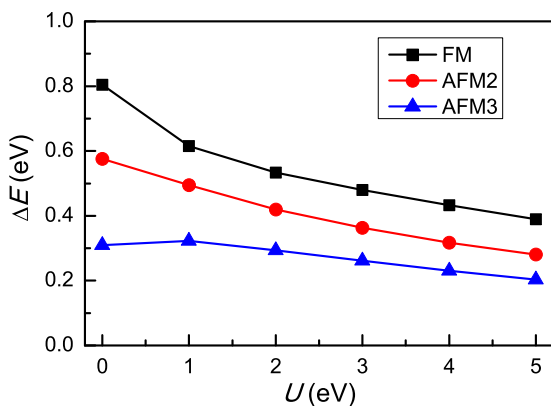


FIG. 5. Energy differences (per unit cell) between FM/AFM2/AFM3 and AFM1 ($E_{\text{AFM1}} = 0$ eV) as a function of U for Mn_2ClF .

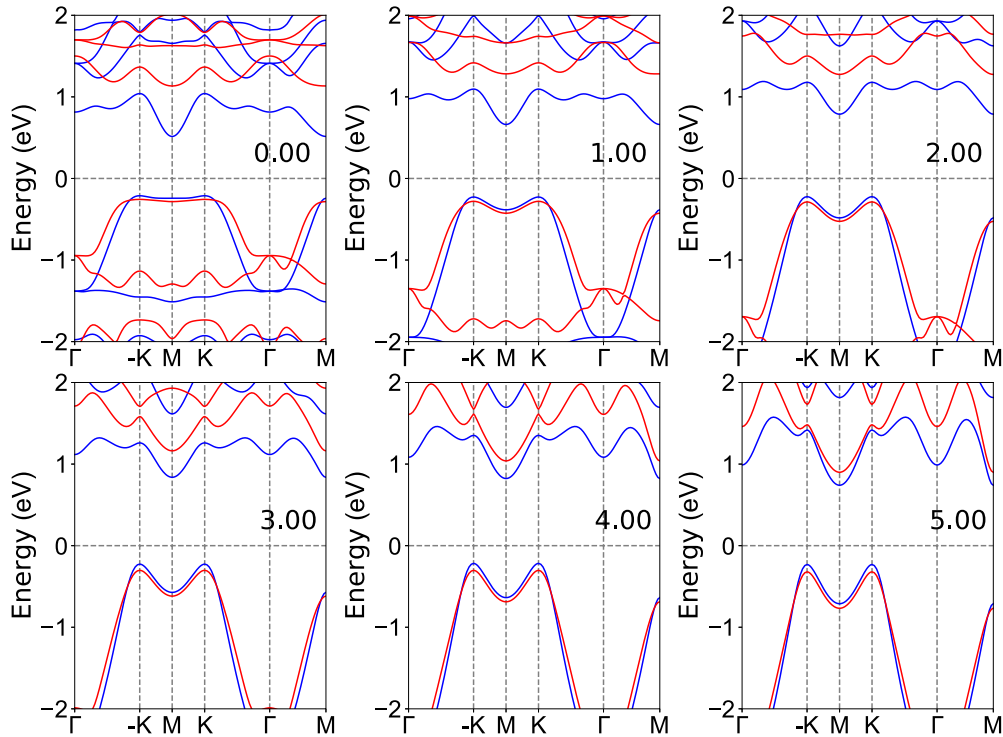


FIG. 6. Band structures of Mn_2ClF at representative U without SOC. The spin-up and spin-down channels are depicted in blue and red.

spin splitting in Mn_2ClF . The piezotronic effect on Rashba spin splitting in a ZnO/P3HT nanowire array structure has been studied experimentally [47], which demonstrates that the Rashba spin splitting can be effectively tuned by an inner-crystal piezopotential created inside the ZnO nanowires. Here the sizable piezoelectric coefficients suggest the possibility of further tuning the spin-splitting effect in Mn_2ClF via the piezoelectric effect.

Discussion and conclusion. Finally, we briefly comment on the possibility of generalizing the mechanism proposed here to 2D altermagnets. For a 2D altermagnet, the magnetic atoms have opposite layer spin polarization (A-type AFM ordering). If the out-of-plane built-in electric field is lacking, the obvious spin splitting in the band structures can still be observed [Figs. 7(a) and 7(b)]. However, the spin-valley polarization is lacking. Recently, spin-valley polarization have been achieved in 2D $\text{Ca}(\text{CoN})_2$ [48] via a generated electric gate field of $0.2 \text{ eV}/\text{\AA}$. For a 2D Janus altermagnet in A-type AFM ordering, the out-of-plane built-in electric field E_b could be used to spontaneously produce spin-valley polarization [Figs. 7(c) and 7(d)]. Such effect is expected to produce staggering bands from different layers, thus leading to additional spin-valley polarization. Here, the out-of-plane electric field is equivalent to an external electric field [49]. The concept proposed here can thus be generalized to a 2D Janus A-type altermagnetic material to yield another mechanism of electric potential difference altermagnet (EPD-AM), which will be explored in a future work.

In summary, we proposed an alternative strategy to obtain spin splitting in a 2D Janus A-type antiferromagnet. Using Mn_2ClF as a dynamically, mechanically, and thermally

stable candidate, we concretely demonstrated the spin-splitting nature of the band structure and further showed that the EPD-AFM is robust against electron correlation in Mn_2ClF . The structural symmetry breaking leads to an out-of-plane piezoelectric response, thus providing a possibility to tune spin splitting in Mn_2ClF by the piezoelectric effect. Due to the intrinsically more energy-saving and fast-operating device applications, the importance of AFM spintronics has been gradually understood in recent years [10,50]. However,

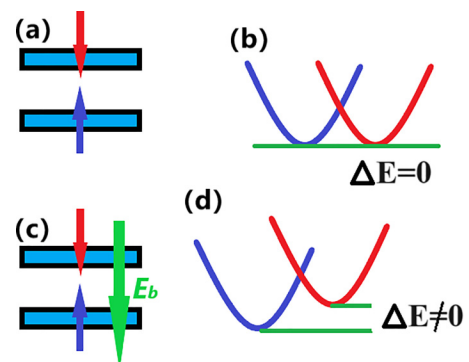


FIG. 7. (a) For a 2D altermagnet, the magnetic atoms have opposite layer spin polarization (A-type antiferromagnetic ordering) without the out-of-plane built-in electric field, destroying the degeneration of electron spin without spin-valley polarization (b). (c) For a 2D Janus altermagnet, the magnetic atoms have opposite layer spin polarization (A-type antiferromagnetic ordering) with the out-of-plane built-in electric field E_b , destroying the degeneration of electron spin with spin-valley polarization (d).

the control and detection of antiferromagnetism remain challenging because of the lack of spin splitting. Our works reveals a 2D family of AFM materials with spontaneous spin splitting, which can be useful for high-speed and high-density spintronic device applications.

Acknowledgments. Y.S.A. is supported by the Singapore Ministry of Education Academic Research Fund Tier 2 (Award No. MOE-T2EP50221-0019). We are grateful to Shanxi Supercomputing Center of China; the calculations were performed on TianHe-2.

-
- [1] I. Žutić, J. Fabian, and S. Das Sarma, *Rev. Mod. Phys.* **76**, 323 (2004).
- [2] J. Nitta, T. Akazaki, H. Takayanagi, and T. Enoki, *Phys. Rev. Lett.* **78**, 1335 (1997).
- [3] A. Manchon, H. C. Koo, J. Nitta, S. M. Frolov, and R. A. Duine, *Nat. Mater.* **14**, 871 (2015).
- [4] E. I. Rashba, *Sov. Phys. Solid State* **2**, 1224 (1960).
- [5] M. I. Dyakonov and V. I. Perel, *Sov. Phys. Solid State* **13**, 3023 (1972).
- [6] B. A. Bernevig, J. Orenstein, and S.-C. Zhang, *Phys. Rev. Lett.* **97**, 236601 (2006).
- [7] J. Schliemann, *Rev. Mod. Phys.* **89**, 011001 (2017).
- [8] P. Altmann, M. P. Walser, C. Reichl, W. Wegscheider, and G. Salis, *Phys. Rev. B* **90**, 201306(R) (2014).
- [9] X. Hu, *Adv. Mater.* **24**, 294 (2012).
- [10] T. Jungwirth, J. Sinova, A. Manchon, X. Marti, J. Wunderlich, and C. Felser, *Nat. Phys.* **14**, 200 (2018).
- [11] L. Šmejkal, J. Sinova, and T. Jungwirth, *Phys. Rev. X* **12**, 031042 (2022).
- [12] I. Mazin, *Phys. Rev. X* **12**, 040002 (2022).
- [13] L. Šmejkal, J. Sinova, and T. Jungwirth, *Phys. Rev. X* **12**, 040501 (2022).
- [14] X. Chen, D. Wang, L. Y. Li, and B. Sanyal, *Appl. Phys. Lett.* **123**, 022402 (2023).
- [15] P. J. Guo, Z. X. Liu, and Z. Y. Lu, *npj Comput. Mater.* **9**, 70 (2023).
- [16] S. D. Guo, X. S. Guo, K. Cheng, K. Wang, and Y. S. Ang, *Appl. Phys. Lett.* **123**, 082401 (2023).
- [17] H.-Y. Ma, M. L. Hu, N. N. Li, J. P. Liu, W. Yao, J. F. Jia, and J. W. Liu, *Nat. Commun.* **12**, 2846 (2021).
- [18] S. Hayami, Y. Yanagi, and H. Kusunose, *Phys. Rev. B* **101**, 220403(R) (2020).
- [19] M. Lee, E. S. Choi, X. Huang, J. Ma, C. R. Dela Cruz, M. Matsuda, W. Tian, Z. L. Dun, S. Dong, and H. D. Zhou, *Phys. Rev. B* **90**, 224402 (2014).
- [20] Y. J. Niu, H. F. Lv, X. J. Wu, and J. L. Yang, *J. Phys. Chem. Lett.* **14**, 4042 (2023).
- [21] P. Hohenberg and W. Kohn, *Phys. Rev.* **136**, B864 (1964); W. Kohn and L. J. Sham, *ibid.* **140**, A1133 (1965).
- [22] G. Kresse, *J. Non-Cryst. Solids* **192-193**, 222 (1995).
- [23] G. Kresse and J. Furthmüller, *Comput. Mater. Sci.* **6**, 15 (1996).
- [24] G. Kresse and D. Joubert, *Phys. Rev. B* **59**, 1758 (1999).
- [25] J. P. Perdew, K. Burke, and M. Ernzerhof, *Phys. Rev. Lett.* **77**, 3865 (1996).
- [26] T. Guo, Y. Liu, Y. Sun *et al.*, *Appl. Phys. Lett.* **122**, 192403 (2023).
- [27] Q. L. Sun and N. Kioussis, *Phys. Rev. B* **97**, 094408 (2018).
- [28] C. Ma, X. J. Chen, K. J. Jin *et al.*, *J. Phys. Chem. Lett.* **14**, 825 (2023).
- [29] Q. Y. Ma, W. H. Wan, Y. M. Li, and Y. Liu, *Appl. Phys. Lett.* **120**, 112402 (2022).
- [30] X. Wu, D. Vanderbilt, and D. R. Hamann, *Phys. Rev. B* **72**, 035105 (2005).
- [31] A. Togo, F. Oba, and I. Tanaka, *Phys. Rev. B* **78**, 134106 (2008).
- [32] L. Zhang, Z. Yang, T. Gong *et al.*, *J. Mater. Chem. A* **8**, 8813 (2020).
- [33] A. Y. Lu, H. Zhu, J. Xiao, C. P. Chuu, Y. Han, M. H. Chiu, C. C. Cheng, C. W. Yang, K. H. Wei, Y. Yang, Y. Wang, D. Sokaras, D. Nordlund, P. Yang, D. A. Muller, M. Y. Chou, X. Zhang, and L. J. Li, *Nat. Nanotechnol.* **12**, 744 (2017).
- [34] J. Zhang, S. Jia, I. Kholmanov, L. Dong, D. Er, W. Chen, H. Guo, Z. Jin, V. B. Shenoy, L. Shi, and J. Lou, *ACS Nano* **11**, 8192 (2017).
- [35] See Supplemental Material at <http://link.aps.org/supplemental/10.1103/PhysRevB.108.L180403> for supporting calculation data and details.
- [36] R. C. Andrew, R. E. Mapasha, A. M. Ukpong, and N. Chetty, *Phys. Rev. B* **85**, 125428 (2012).
- [37] W. Y. Tong, S. J. Gong, X. Wan, and C. G. Duan, *Nat. Commun.* **7**, 13612 (2016).
- [38] P. Jiang, X. H. Zheng, L. L. Kang, X. X. Tao, H. M. Huang, X. C. Dong, and Y. L. Li, *J. Mater. Chem. C* **11**, 2703 (2023).
- [39] S. D. Guo, J. X. Zhu, M. Y. Yin, and B. G. Liu, *Phys. Rev. B* **105**, 104416 (2022).
- [40] S. D. Guo, W. Q. Mu, and B. G. Liu, *2D Mater.* **9**, 035011 (2022).
- [41] S. D. Guo, Y. L. Tao, W. Q. Mu, and B. G. Liu, *Front. Phys.* **18**, 33304 (2023).
- [42] S. Li, Q. Q. Wang, C. M. Zhang, P. Guo, and S. A. Yang, *Phys. Rev. B* **104**, 085149 (2021).
- [43] W. Y. Pan, *Phys. Rev. B* **106**, 125122 (2022).
- [44] L. Dong, J. Lou, and V. B. Shenoy, *ACS Nano* **11**, 8242 (2017).
- [45] M. N. Blonsky, H. L. Zhuang, A. K. Singh, and R. G. Hennig, *ACS Nano* **9**, 9885 (2015).
- [46] K. N. Duerloo, M. T. Ong, and E. J. Reed, *J. Phys. Chem. Lett.* **3**, 2871 (2012).
- [47] L. Zhu, Y. Zhang, P. Lin *et al.*, *ACS Nano* **12**, 1811 (2018).
- [48] R. W. Zhang, C. X. Cui, R. Z. Li, J. Y. Duan, L. Li, Z. M. Yu, and Y. G. Yao, [arXiv:2306.08902](https://arxiv.org/abs/2306.08902).
- [49] A. O. Fumega and J. L. Lado, *Nanoscale* **15**, 2181 (2023).
- [50] T. Jungwirth, X. Marti, P. Wadley, and J. Wunderlich, *Nat. Nanotechnol.* **11**, 231 (2016).